

Total pressure fluctuations and two-phase flow turbulence in hydraulic jumps

Hang Wang · Frédéric Murzyn · Hubert Chanson

Received: 31 July 2014 / Revised: 30 September 2014 / Accepted: 19 October 2014 / Published online: 5 November 2014
 © Springer-Verlag Berlin Heidelberg 2014

Abstract The large-scale turbulence and high air content in a hydraulic jump restrict the application of many traditional flow measurement techniques. This paper presents a physical modelling of hydraulic jump, where the total pressure and air–water flow properties were measured simultaneously with intrusive probes, namely a miniature pressure transducer and a dual-tip phase-detection probe, in the jump roller. The total pressure data were compared to theoretical values calculated based upon void fraction, water depth and flow velocity measured by the phase-detection probe. The successful comparison showed valid pressure measurement results in the turbulent shear region with constant flow direction. The roller region was characterised by hydrostatic pressure distributions, taking into account the void fraction distributions. The total pressure fluctuations were related to both velocity fluctuations in the air–water flow and free-surface dynamics above the roller, though the time scales of these motions differed substantially.

List of symbols

C	Time-averaged void fraction
C_{\max}	Local maximum time-averaged void fraction in the shear flow region
$D^\#$	Dimensionless diffusivity in the turbulent shear region

D^*	Dimensionless diffusivity in the free-surface region
d_1	Inflow water depth immediately upstream of the jump toe (m)
F	Bubble count rate (Hz)
F_{clu}	Longitudinal bubble cluster count rate (Hz)
$(F_{\text{clu}})_{\max}$	Maximum cluster count rate in the shear flow region (Hz)
F_{fs}	Characteristic free-surface fluctuation frequency (Hz)
F_{\max}	Maximum bubble count rate in the shear flow region (Hz)
$F_p^{(H)}$	Upper total pressure fluctuation frequency (Hz)
$F_p^{(L)}$	Lower total pressure fluctuation frequency (Hz)
Fr_1	Inflow Froude number, $Fr_1 = V_1 / \sqrt{g \times d_1}$
g	Gravity acceleration (m/s^2)
h	Upstream gate opening (m)
L_r	Length of jump roller (m)
P	Time-averaged total pressure (Pa)
P_k	Kinetic pressure (Pa)
P_{\max}	Maximum mean total pressure in the shear flow region (Pa)
P_o	Piezometric pressure (Pa)
p'	Standard deviation of total pressure (Pa)
p'_{\max}	Maximum total pressure fluctuation (Pa)
Q	Flow rate (m^3/s)
Re	Reynolds number, $Re = \rho \times V_1 \times d_1 / \mu$
T	Time lag for maximum cross-correlation coefficient (s)
$T_{0.5}$	Time lag for auto-correlation coefficient being 0.5 (s)
Tu	Turbulence intensity
Tu''	Decomposed turbulence intensity of high-frequency signal component

H. Wang (✉) · H. Chanson
 School of Civil Engineering, The University of Queensland,
 Brisbane, QLD 4072, Australia
 e-mail: hang.wang@uqconnect.edu.au

F. Murzyn
 ESTACA Campus Ouest, Parc Universitaire de Laval Changé,
 BP 53061, Laval Cedex 9, France

U	Free-stream velocity in upstream supercritical flow (m/s)
V	Average air–water interfacial velocity (m/s)
V_{\max}	Maximum interfacial velocity in the shear flow region (m/s)
V_{recirc}	Average recirculation velocity in the free-surface region (m/s)
V_1	Average inflow velocity (m/s)
v'	Standard deviation of interfacial velocity (m/s)
W	Channel width (m)
x	Longitudinal distance from the upstream gate (m)
x_1	Longitudinal position of jump toe (m)
$Y_{C\max}$	Characteristic elevation of local maximum void fraction in the shear region (m)
$Y_{F\max}$	Characteristic elevation of maximum bubble count rate in the shear region (m)
$Y_{P\max}$	Characteristic elevation of maximum mean total pressure in the shear region (m)
$Y_{p'\max}$	Characteristic elevation of maximum total pressure fluctuation in the shear region (m)
$Y_{V\max}$	Characteristic elevation of maximum interfacial velocity in the shear region (m)
$Y_{0.5}$	Characteristic elevation of half maximum interfacial velocity (m)
Y_{50}	Characteristic elevation where $C = 0.5$ (m)
Y_{90}	Characteristic elevation where $C = 0.9$ (m)
y	Vertical distance from the channel bed (m)
y^*	Characteristic elevation of local minimum void fraction (m)
z	Transverse distance from the channel centreline (m)
Δx	Longitudinal separation distance between two phase-detection probe sensors (m)
δ	Inflow boundary-layer thickness at channel bed (m)
μ	Water dynamic viscosity ($\text{Pa} \times \text{s}$)
ρ	Water density (kg/m^3)
τ	Time lag (s)
$\tau_{0.5}$	Time lag between maximum and half maximum cross-correlation coefficients (s)

1 Introduction

A hydraulic jump is a rapidly varied open channel flow characterised by a sudden transition from a supercritical flow motion to a subcritical regime. The jump toe, where the upstream flow impinges into the downstream region, is a singular locus with discontinuity in velocity and pressure fields (Rajaratnam 1967). The transition region

immediately downstream of the toe is named the jump roller because of the presence of large-scale vortices and flow recirculation. The jump roller is a turbulent two-phase flow region with coexistence of and interaction between air entrainment, turbulence and flow instabilities.

The turbulent nature of hydraulic jump leads to an efficient energy dissipation rate. For example, an inflow Froude number $Fr_1 = 9$ gives a theoretical energy dissipation rate exceeding 70 %, where the Froude number is defined as $Fr_1 = V_1 \times (g \times d_1)^{-1/2}$, V_1 being the average inflow velocity and d_1 the inflow depth. Therefore, hydraulic jumps are often generated in hydraulic structures for the purpose of energy dissipation (Fig. 1). However, the large shear force and fluctuating motions of the flow may challenge the strength of construction, e.g. on the bottom of the jump in a stilling basin. In the early 20th century, the attention to hydraulic jump was first triggered with the design of energy dissipators, which was developed by USBR (US Bureau of Reclamation) in 1940s and 1950s (Riegel and Beebe 1917; Peterka 1958). A number of studies contributed to the pressure quantification mainly beneath hydraulic jumps (Vasiliev and Bukreyev 1967; Schiebe 1971; Abdul Khader and Elango 1974; Lopardo and Henning 1985; Fiorotto and Rinaldo 1992; Lopardo and Romagnoli 2009). The relationship between cavitation occurrence and pressure fluctuations was investigated (Narayanan 1980). The pressure fluctuations were further correlated with water level fluctuations and/or velocity turbulence in some limited flow conditions with minor aeration (Onitsuka et al. 2009; Lopardo 2013).

In most prototype conditions with large inflow Froude number, the air entrainment in hydraulic jump is significant. Air entrapped at the jump toe as well as through the rough roller surface is advected downstream by large vortical structures (Long et al. 1991). The diffusive advection of air bubbles interplays with the turbulence development. The studies of two-phase flow properties were represented by Rajaratnam (1962), Resch and Leuthesser (1972) and Chanson (1995) describing the air concentration and interfacial velocity characteristics using air–water interface detection techniques. The turbulence characterisation was promoted by Chanson and Toombes (2002) and Chanson and Carosi (2007) and recently developed by Wang et al. (2014) based upon statistical analysis of interface detection signals. In a few attempts of numerical modelling, the air entrainment was rarely taken into account together with the dynamic features of the flow (Richard and Gavriluk 2013). Physical modelling with consideration of simultaneous air entrainment and flow turbulence/fluctuations included Cox and Shin (2003), Murzyn and Chanson (2009) and Wang and Chanson (2014).

Fig. 1 Prototype and physical modelling of hydraulic jumps. **a** Hydraulic jump downstream of a salt water intrusion prevention weir at Jungmun, Jeju Island, Korea (2013). **b** Experimental hydraulic jump in horizontal rectangular channel. Flow from left to right. Flow conditions: $Q = 0.0461 \text{ m}^3/\text{s}$, $d_1 = 0.032 \text{ m}$, $x_1 = 1.25 \text{ m}$, $Fr_1 = 5.1$, $Re = 9.1 \times 10^4$



Direct pressure measurement in hydraulic jump flows with strong air entrainment is lacking despite the significance in hydraulic engineering. This paper presents new experiments measuring the total pressure distributions within the jump roller. The air–water flow properties were characterised at the adjacent locations, and the water level fluctuations above were recorded as well. The application of total pressure transducer in such turbulent bubbly flow was justified by a comparison between the total pressure output and calculations based upon air–water flow measurement results. The present work provides new information on the flow regime and fluctuating nature of hydraulic jumps and allows further investigation on the interactions between turbulence, aeration and flow instabilities in such a flow.

2 Physical modelling and instrumentation

2.1 Dimensional considerations

Any theoretical and numerical analyses of hydraulic jumps are based upon a large number of relevant equations to

describe the two-phase turbulent flow motion and the interaction between entrained air and turbulence. The outputs must be tested against a broad range of gas–liquid flow measurements: ‘Unequivocally [...] no experimental data means no validation’ (Roache 2009). Physical modelling requires the selection of a suitable dynamic similarity (Liggett 1994). Considering a hydraulic jump in a smooth horizontal rectangular channel, dimensional considerations give a series of dimensionless relationships in terms of the turbulent two-phase flow properties at a position (x, y, z) within the hydraulic jump roller as functions of the inflow properties, fluid properties and channel configurations. Using the upstream flow depth d_1 as the characteristic length scale, a dimensional analysis yields

$$\frac{P}{0.5 \times \rho \times V_1^2}, \frac{p'}{0.5 \times \rho \times V_1^2}, \frac{V}{V_1}, \frac{v'}{V_1}, C, \frac{F \times d_1}{V_1}, \dots = F\left(\frac{x-x_1}{d_1}, \frac{y}{d_1}, \frac{z}{d_1}, Fr_1, Re, \frac{v'_1}{V_1}, \frac{x_1}{d_1}, \frac{W}{d_1}, \dots\right) \quad (1)$$

where P and V are the total pressure and velocity, respectively, p' and v' are pressure and velocity fluctuations, C is the void fraction, F is the bubble count rate, x_1 is

the jump toe position, Re is the Reynolds number, W is the channel width and the subscript 1 refers to the inflow conditions. In a hydraulic jump, the momentum considerations demonstrated the significance of the inflow Froude number, and the selection of the Froude similitude derives implicitly from basic theoretical considerations (Lighthill 1978; Liggett 1994). Equation (1) shows that measurements in small size models might be affected by viscous scale effects because the Reynolds number is grossly underestimated. In the present study, the experiments were performed in a relatively large-size facility to minimise scale effects (Murzyn and Chanson 2008; Chanson and Chachereau 2013).

2.2 Experimental set-up and flow conditions

The experimental channel was 3.2 m long and 0.5 m wide, built with horizontal HDPE bed and 0.4-m high glass sidewalls (Fig. 1b). The inflow was supplied to the flume from a constant head tank. A rounded undershoot gate of the head tank induced a horizontal impinging flow without contraction. The gate opening was set at $h = 0.02$ m, and hydraulic jumps were generated at $x_1 = 0.83$ m downstream of the gate. The inflow depth was measured using a point gauge right upstream of the jump toe. The tailwater depth and jump toe position were controlled by an overshoot gate at the end of the channel. The flow rate was measured with a Venturi meter in the supply line. While the flow rate measurement was within an accuracy of 2 %, the precision of the determination of inflow depth and jump toe position relied largely on the fluctuation level of the flow.

Four inflow Froude numbers $Fr_1 = 3.8, 5.1, 7.5$ and 8.5 were tested, corresponding to Reynolds numbers $3.5 \times 10^4 < Re < 8.0 \times 10^4$. The total pressure and two-phase flow properties were measured locally with intrusive total pressure probe and phase-detection probe. The probes were placed side by side with a 9-mm transverse distance between the sensor tips and sampled at a number of elevations in a vertical cross-section on the channel centreline. The instantaneous water elevation above the measurement location was measured non-intrusively with an acoustic displacement meter. The instrumental set-up is illustrated in Fig. 2, and the flow conditions are summarised in Table 1 along with the longitudinal positions of the scanned cross-sections. With an inflow length $x_1/h = 41.5$, the inflow conditions were characterised by partially developed boundary layer at the channel bed ($\delta/d_1 < 1$ at $x = x_1$, Table 1, 7th column). Figure 3a presents typical inflow velocity profiles measured with a Prandtl–Pitot tube along the channel centreline. A developing boundary layer was shown with a constant free-stream velocity U . Figure 3b compares the free-stream velocity U with the average inflow velocity V_1 for a broader range of flow

conditions. The results indicated $U \approx 1.1 \times V_1$ because the velocities in boundary layers were lower than the cross-sectional average. Resch and Leutheusser (1972) and Thandaveswara (1974) compared the air–water flow properties for different types of inflow conditions (partially developed, fully developed and per-entrained). The presence of highly aerated shear flow region (see Sect. 3.2.1 below) was only observed for partially developed inflow conditions, with the shortest aeration length downstream of the toe (Chanson 1997).

2.3 Instrumentation

The total pressure probe consisted of a silicon diaphragm sensor mounted on the probe tip. The sensor was a miniature Micro-Electro-Mechanical-System technology-based pressure transducer (Model MRV21, by MeasureX, Australia). Such a diaphragm pressure sensor is not affected by the presence of bubbles and does not require to be purged. The sensor had a 5-mm outer diameter with 4-mm-diameter sensor. The model provided a measurement range between 0 and 1.5 bars (absolute pressures). The response frequency was in excess of 100 kHz. The sampling frequency was set at 5 kHz in the present study, though the signal was filtered by a signal amplification system to eliminate noises above 2 kHz. A daily calibration was conducted and regularly checked, because the output voltage appeared to be temperature and ambient-pressure sensitive. The largest uncertainty of the total pressure measurements was thought to be introduced by the fluctuations in atmospheric pressure reading.

The dual-tip phase-detection probe was designed to pierce bubbles and droplets with its two needle sensors and worked based upon the difference in electrical resistance between air and water. The needle sensor tips (0.25 mm inner diameter) were separated longitudinally by $\Delta x = 7.25$ mm. While the signal of each sensor gave the local void fraction and bubble count rate data, a cross-correlation between the signals provided an average time T of the air–water interfaces travelling over the distance Δx , yielding a mean longitudinal interfacial velocity $V = \Delta x/T$. The phase-detection probe was excited by an electronic system designed with a response time $< 10 \mu s$ and scanned at 5 kHz simultaneously with the total pressure probe and an acoustic displacement meter above the probe leading tip. A MicrosonicTM Mic+25/IU/TC acoustic displacement meter measured the instantaneous water elevation with a 20-Hz response time which was lower than the sampling rate. The sensor height was carefully adjusted to ensure that the displacement meter measurement range covered the maximum free-surface fluctuations, and the erroneous samples caused by splashing droplets were removed from the signal.

Fig. 2 Instrumentation set-up and photograph of side-by-side dual-tip phase-detection probe and total pressure probe (views in elevation)

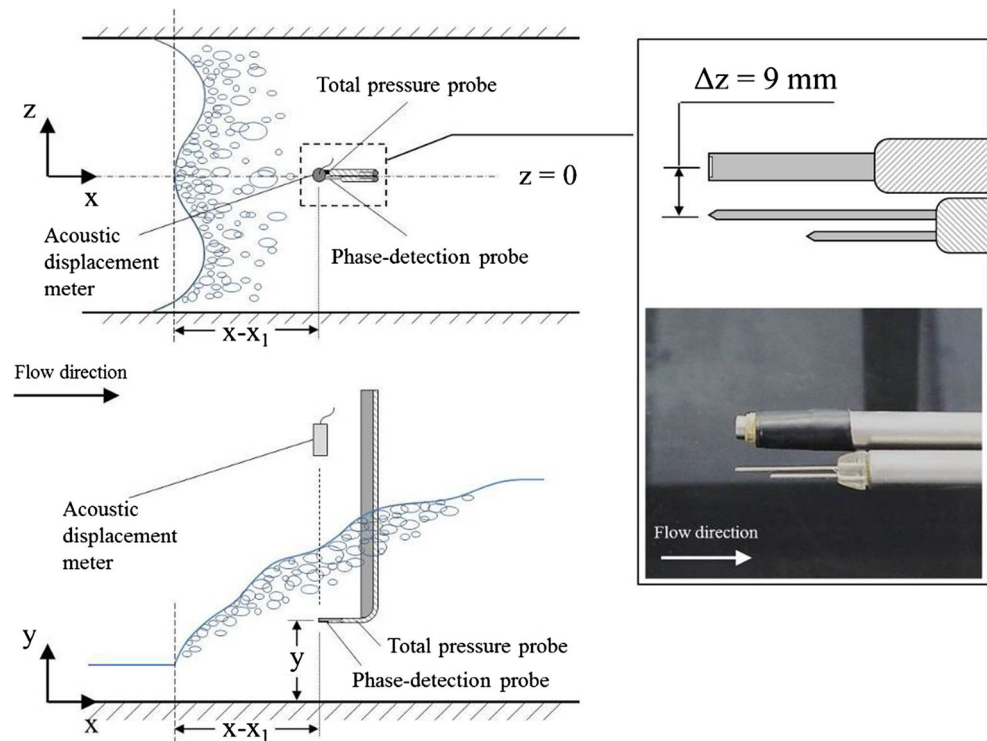


Table 1 Experimental flow conditions and longitudinal locations of measurement cross-sections

Q (m ³ /s)	W (m)	h (m)	x_1 (m)	d_1 (m)	V_1 (m/s)	δ/d_1 (—)	U (m/s)	Fr_1 (—)	Re (—)	$(x - x_1)/d_1$ (—)			
0.0179	0.5	0.02	0.83	0.0206	1.74	0.845	1.85	3.8	3.5×10^4	4.15	8.35	12.5	
0.0239	0.5	0.02	0.83	0.0209	2.29	0.735	2.45	5.1	4.8×10^4	4.15	8.35	12.5	18.75
0.0347	0.5	0.02	0.83	0.0206	3.37	0.700	3.50	7.5	6.8×10^4	4.15	8.35	12.5	18.75
0.0397	0.5	0.02	0.83	0.0208	3.82	0.765	4.10	8.5	8.0×10^5	4.15	8.35	12.5	18.75

Q flow rate, W channel width, h upstream gate opening, x_1 longitudinal jump toe position, d_1 inflow depth, V_1 average inflow velocity, δ inflow boundary-layer thickness, U upstream free-stream velocity, Fr_1 inflow Froude number, Re inflow Reynolds number

The simultaneous sampling of all instruments was performed for 180 s at each measurement location.

3 Results

3.1 Basic flow patterns

Observations showed some enhanced flow aeration and turbulent fluctuations with increasing Froude number. The large-scale turbulent structures inside the roller were visualised by the entrained air bubbles (Fig. 1b). The formation of large turbulent structures was linked to the oscillations of jump toe position and free-surface fluctuations (Long et al. 1991; Wang et al. 2014). These motions were observed in a pseudo-periodic manner, together with the associated air

entrapment and macroscopic variation in velocity and pressure fields. For instance, the slow pressure pulsations could be felt by placing a hand in the roller. Basically, the pulse of increasing impinging pressure appeared to correspond to the downstream ejection of large vortices.

The water elevation measured along the channel centreline outlined the time-averaged free-surface profiles similar to the visual observations. The length of hydraulic jump roller L_r is defined as the longitudinal distance over which the water elevation increases monotonically. The roller length was derived from the free-surface profile and found to be an increasing function of the Froude number. A linear relationship was given by the data set consisting of Murzyn et al. (2007), Kucukali and Chanson (2008), Murzyn and Chanson (2009), Wang and Chanson (2014) and the present study:

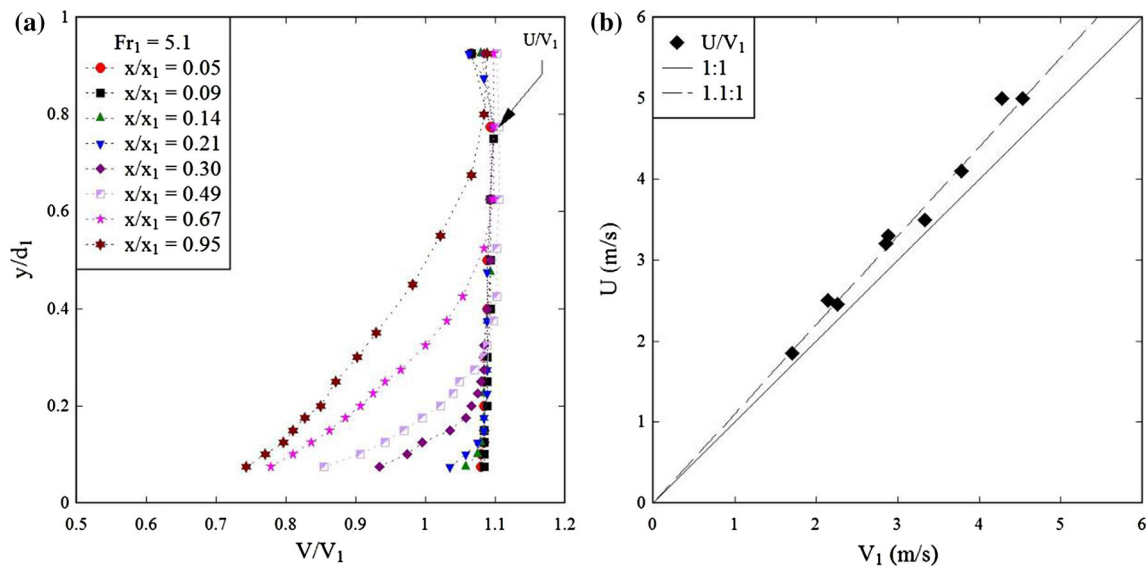


Fig. 3 Inflow conditions. **a** Inflow velocity profiles on the channel centreline—flow conditions: $Q = 0.0239 \text{ m}^3/\text{s}$, $d_1 = 0.0209 \text{ m}$, $x_1 = 0.83 \text{ m}$, $Fr_1 = 5.1$, $Re = 4.8 \times 10^4$. **b** Comparison between

inflow free-stream velocity U and average inflow velocity V_1 for $3.8 < Fr_1 < 10$, $3.4 \times 10^4 < Re < 1.6 \times 10^5$

$$\frac{L_r}{d_1} = 6 \times (Fr_1 - 1) \quad \text{for } 2 < Fr_1 < 10 \quad (2)$$

The free-surface profile was self-similar over the roller length ($0 < x - x_1 < L_r$) for different flow conditions.

3.2 Two-phase flow properties

3.2.1 Void fraction

The time-averaged void fraction data were measured with 5 kHz sampling rate for 180 s, and they showed consistent results with previous measurements at 20 kHz for 45 s (Wang and Chanson 2014). Figure 4 shows a comparison between the vertical void fraction distributions in the present study and Wang and Chanson (2014) for identical flow conditions and longitudinal positions. The typical void fraction profile exhibited a bell-shape distribution in the turbulent shear region, with a local maximum C_{\max} at the vertical position $Y_{C_{\max}}$, and a rapid increase to unity in the free-surface region. The boundary between the turbulent shear region and free-surface region was characterised by the local minimum in void fraction at the elevation y^* which increased along the roller. The bell-shape void fraction profile corresponded to the singular air entrainment at the jump toe and advective diffusion of bubbles in the shear layer. The experimental data fitted a solution of classical two-dimensional diffusion equation (Crank 1956; Chanson 1995):

$$C = C_{\max} \times \exp \left(-\frac{1}{4 \times D^{\#}} \times \frac{\left(\frac{y - Y_{C_{\max}}}{d_1} \right)^2}{\left(\frac{x - x_1}{d_1} \right)} \right) \quad 0 < y < y^* \quad (3)$$

where $D^{\#}$ is a dimensionless diffusivity. $D^{\#}$ was typically between 0.02 and 0.1 and increased with increasing distance between the measurement cross-section and jump toe. The local maximum void fraction C_{\max} and its elevation $Y_{C_{\max}}$ were given by the experimental data. The value of C_{\max} decreased from about 0.5 at the jump toe ($x = x_1$) to below 0.05 at the end of roller ($x - x_1 = L_r$), while the elevation of $Y_{C_{\max}}$ increased, leading to a broadened void fraction profile. The increase in $Y_{C_{\max}}$ reflected the buoyancy effects on the bubble diffusion as well as the enlargement of highly aerated large-scale vortices. On the other hand, the monotonic increase in void fraction through the free-surface region ($y > y^*$) corresponded to the interfacial air–water exchange. The data fitted a Gaussian error function (Brattberg et al. 1998; Murzyn et al. 2005):

$$C = \frac{1}{2} \times \left(1 + \operatorname{erf} \left(\frac{y - Y_{50}}{2 \times \sqrt{\frac{D^* \times (x - x_1)}{V_1}}} \right) \right) \quad y > y^* \quad (4)$$

where Y_{50} is the characteristic elevation in the free-surface region with $C = 0.5$ and D^* is a dimensionless diffusivity ranging between 1×10^{-4} and 6×10^{-3} and decreased with increasing distance from the toe. Equations (3) and (4) are plotted in Fig. 4 for the given void fraction data.

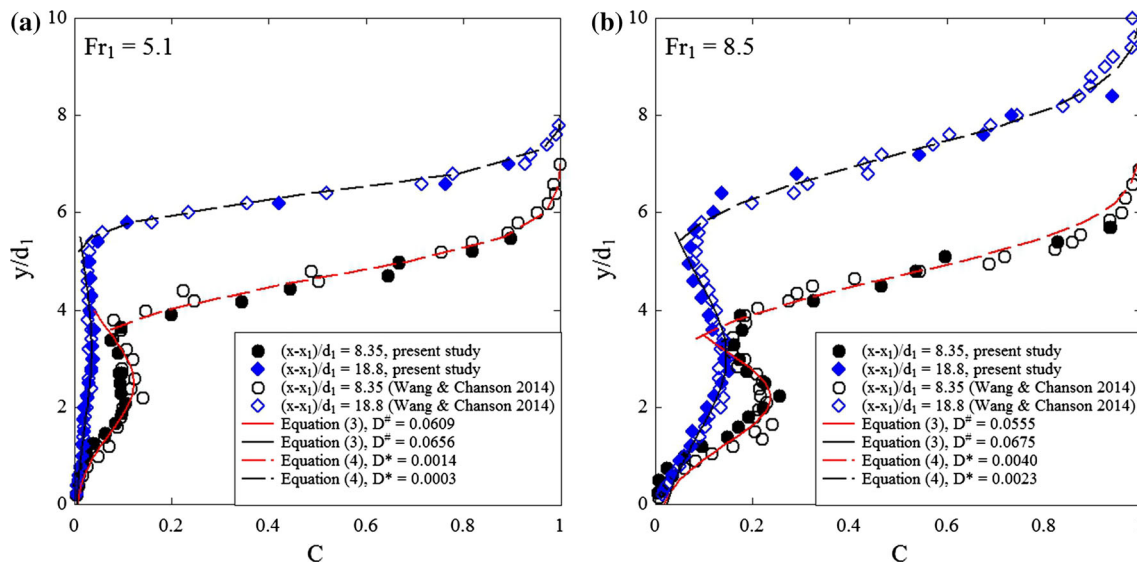


Fig. 4 Vertical distributions of time-averaged void fraction at two longitudinal positions in jump roller—comparison with data of Wang and Chanson (2014) and Eqs. (3) and (4). **a** $Fr_1 = 5.1$. **b** $Fr_1 = 8.5$

3.2.2 Bubble and bubble cluster count rates

The bubble count rate equals half of the total number of air–water (and water–air) interfaces detected per unit time. It reflected the flux of bubbles or droplets, hence the air–water interfacial area for a given void fraction. The bubble count rate was directly linked to the shear stress relative to the air–water surface tension. Figure 5 shows the vertical bubble count rate distributions for the same flow conditions in Fig. 4, and the maximum bubble count rates F_{\max} can be seen in the turbulent shear region where the shear stress was maximum. F_{\max} decreased rapidly along the jump roller as the shear flow region was de-aerated. A local minimum was shown between the maximum bubble count rate F_{\max} and a secondary peak next to the free surface at the same elevation y^* of the local minimum void fraction. The present data measured at 5 kHz for 180 s are compared with the data of Wang and Chanson (2014) measured using the same instrumentation at 20 kHz for 45 s. Almost the same results were obtained for the smaller Froude number (Fig. 5a), while differences were seen for the higher Froude number in terms of F_{\max} (Fig. 5b). The smaller bubble count rate given by the lower sampling frequency was caused by the non-detection of the class of smallest air bubbles. This difference was significant when the Froude number and Reynolds number were large and when the turbulent shear level was high, because a large number of very fine bubbles were advected at high velocity. Sensitivity analyses indicated that the sampling rate of 20 kHz was adequate for the given instrumental size (Toombes 2002), and it is acknowledged that the present sampling rate was slower.

The instantaneous bubble distribution was highly affected by the turbulent flow structures, and bubbles tended to travel in clusters rather than in randomness (Chanson 2007). Though a bubble cluster was spatially three-dimensional, some simplistic analysis of one-dimensional clusters in the longitudinal direction could provide basic information on the clustering behaviour. Herein, the longitudinal bubble clusters were identified using a near-wake criterion in the bubbly flow with $C < 0.3$. That is, two bubbles were considered in a cluster when their interval time was smaller than the time that the leading bubble spent on the probe sensor tip. The near-wake criterion implied that the trailing bubble in a cluster was in the wake of the leading bubble. Figure 5 includes the distributions of cluster count rate F_{clu} , showing similar profile shapes as the bubble count rates with $F_{\text{clu}} < F$. The results simply indicated more clusters for a larger number of bubbles. The clustering properties might describe the air–turbulence interaction at some larger length-scale level compared to the basic air–water flow properties. The maximum cluster count rate $(F_{\text{clu}})_{\max}$ decreased in a larger rate along the roller than the maximum bubble count rate F_{\max} , implying a faster dispersion of turbulent structures compared to the de-aeration process.

3.2.3 Interfacial velocity and turbulence intensity

The time-averaged air–water interfacial velocity V was derived from a cross-correlation analysis of the dual-tip phase-detection probe signals. Assuming a random detection of infinitely large number of air–water interfaces, the turbulence intensity Tu was further calculated as:

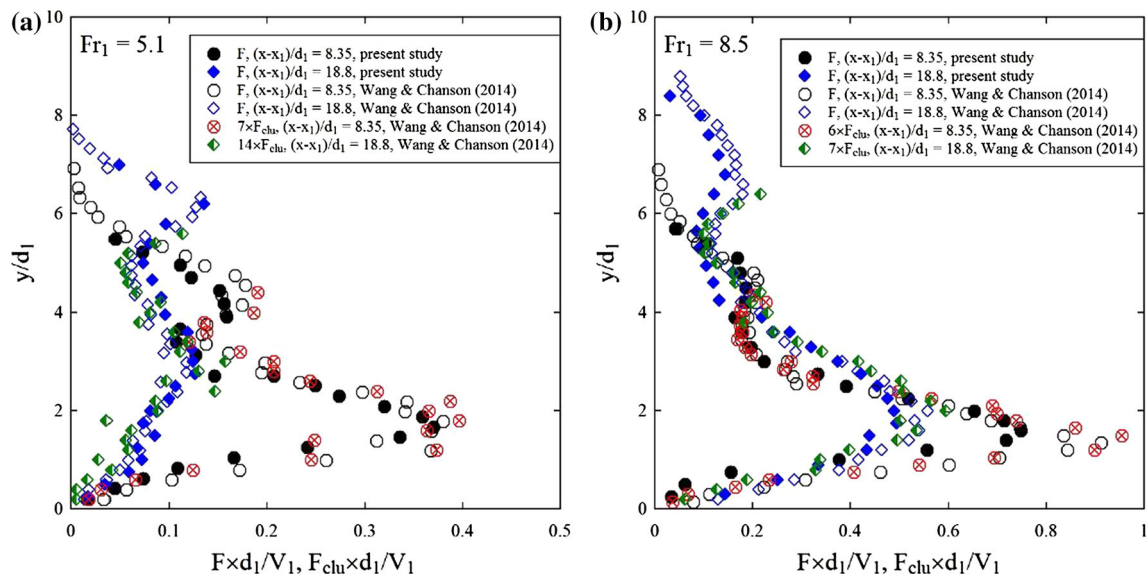


Fig. 5 Vertical distributions of bubble count rate at two longitudinal positions in jump roller—comparison with bubble count rate and bubble cluster count rate (for $C < 0.3$) of Wang and Chanson (2014). **a** $Fr_1 = 5.1$. **b** $Fr_1 = 8.5$

$$Tu = 0.851 \times \frac{\sqrt{\tau_{0.5}^2 - T_{0.5}^2}}{|T|} \quad (5)$$

where T is the time lag of maximum cross-correlation coefficient, $\tau_{0.5}$ is the time lag between the maximum and half maximum cross-correlation functions, and $T_{0.5}$ is the time lag of half maximum auto-correlation function of the leading sensor signal (Chanson and Toombes 2002). Because the turbulent motion of air–water interfaces was a combination of fast velocity turbulence and relatively slow fluctuating motions of the flow, Eq. (5) often gives unusually large turbulence intensities in the flow region where the impact of large-scale fluctuations was significant. Wang et al. (2014) identified the respective contributions of fast and slow turbulent motions by decomposing the phase-detection signal into the mean, low-frequency and high-frequency components. The turbulence intensity Tu'' deduced from the high-frequency signal component reflected the ‘true’ turbulence of the flow.

Figure 6 presents the distributions of time-averaged interfacial velocity, turbulence intensities Tu given by the raw phase-detection probe signal and Tu'' by the high-frequency signal component (>10 Hz) for $Fr_1 = 7.5$ in the jump roller. The upper limit of two-phase flow region was outlined with the characteristic elevation Y_{90} where the time-averaged void fraction $C = 0.9$. Positive velocities were observed in the turbulent shear region, with a maximum V_{max} close to the channel bed. A quasi-uniform negative velocity characterised the flow recirculation next to the free surface. Note that the effect of the probe orientation was limited for the recirculation velocity

measurement. Physically meaningful data were absent in the transition area between positive and negative velocity regions because of the limitation of the cross-correlation technique.

In the lower turbulent shear region where the void fraction increased monotonically, the turbulence intensity Tu increased gradually with increasing distance normal to the invert. Above this region, Tu became large corresponding to the periodic presence of large vortical structures in the upper shear layer and free-surface fluctuations in the recirculation region. The decomposed high-frequency turbulence intensity Tu'' was consistently smaller than Tu and almost uniform in a vertical cross-section. For the given flow conditions in Fig. 6, the high-frequency turbulence intensity was about 1 close to the jump toe and decreased in the streamwise direction. The difference between Tu'' and Tu indicated considerable impact of slow fluctuating motions of the flow on the turbulence characterisation (Wang et al. 2014).

An analogy between a wall jet and the impinging flow into the jump roller suggested a velocity distribution following some wall jet equation (Rajaratnam 1965):

$$\frac{V}{V_{max}} = \left(\frac{y}{Y_{V_{max}}} \right)^{\frac{1}{n}} \quad \text{for } \frac{y}{Y_{V_{max}}} < 1 \quad (6a)$$

$$\frac{V - V_{recirc}}{V_{max} - V_{recirc}} = \exp \left(-\frac{1}{2} \times \left(1.765 \times \left(\frac{y - Y_{V_{max}}}{Y_{0.5}} \right) \right)^2 \right) \quad \text{for } \frac{y}{Y_{V_{max}}} > 1 \quad (6b)$$

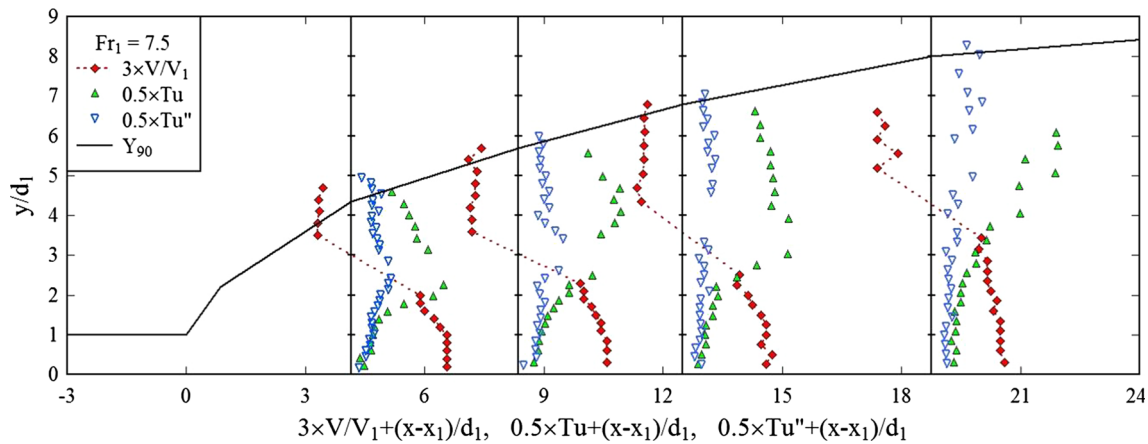


Fig. 6 Vertical distributions of time-averaged interfacial velocity, turbulence intensities Tu derived from raw phase-detection probe signal and Tu'' from high-frequency signal component—flow conditions: $Q = 0.0347 \text{ m}^3/\text{s}$, $d_1 = 0.0206 \text{ m}$, $x_1 = 0.83 \text{ m}$, $Fr_1 = 7.5$, $Re = 6.8 \times 10^4$

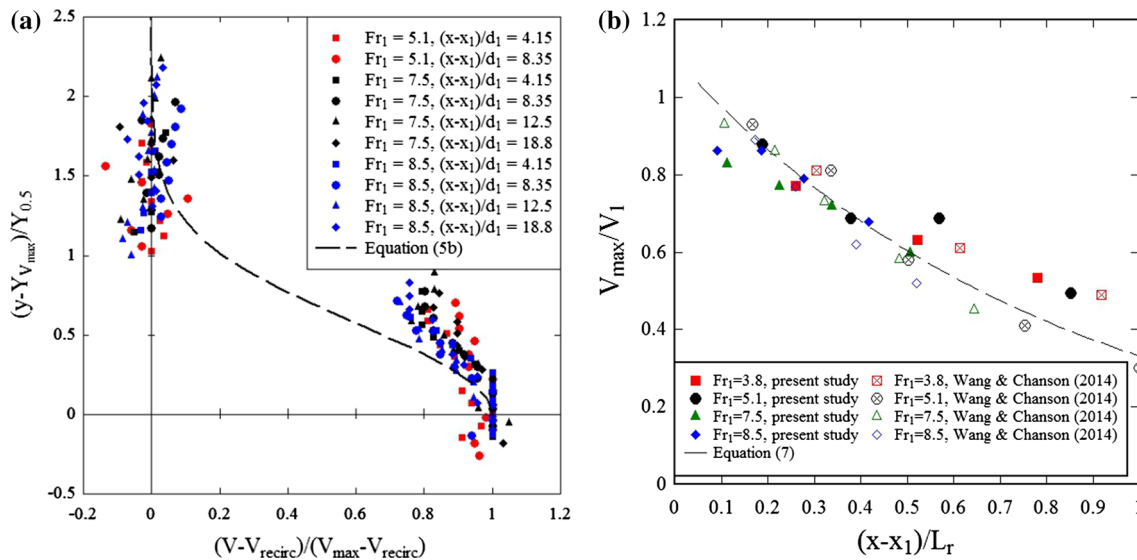


Fig. 7 Vertical distributions of interfacial velocity and longitudinal decay of its maximum. **a** Self-similar interfacial velocity profile with comparison to Eq. (6b). **b** Maximum interfacial velocity as a function

where V_{recirc} is the average recirculation velocity, $Y_{0.5}$ is the elevation where $V = V_{\text{max}}/2$, N is a constant between 6 and 10, and a no-slip condition is applied at the channel bed. Equation (6) depicts a self-similar velocity distribution in a hydraulic jump with a marked roller. All velocity data with $V_{\text{recirc}} < 0$ are presented in Fig. 7a and compared to Eq. (6b). The maximum velocity V_{max} in the turbulent shear region decreased with increasing distance from the toe. The longitudinal decay is shown in Fig. 7b and compared with the data of Wang and Chanson (2014). Altogether the data followed a constant decay trend within the roller length L_r :

$$\frac{V_{\text{max}}}{V_1} = 1.1 \times \exp\left(-1.2 \times \frac{x - x_1}{L_r}\right) \quad (7)$$

of the longitudinal position—comparison with the data of Wang and Chanson (2014) and Eq. (7)

Considering the upstream free-stream velocity $U = 1.1 \times V_1$ and Eq. (2), the longitudinal decrease in maximum interfacial velocity was expressed as:

$$V_{\text{max}} = U \times \exp\left(-\frac{1}{5 \times (Fr_1 - 1)} \times \frac{x - x_1}{d_1}\right) \quad (8)$$

3.3 Total pressure in turbulent shear region

In the horizontal channel, the total pressure P was the sum of the piezometric pressure P_o and the kinetic pressure P_k :

$$P(y) = P_o(y) + P_k(y) \quad (9)$$

The piezometric pressure was a function of the flow depth and relative measurement elevation, while the kinetic pressure was a function of the local velocity:

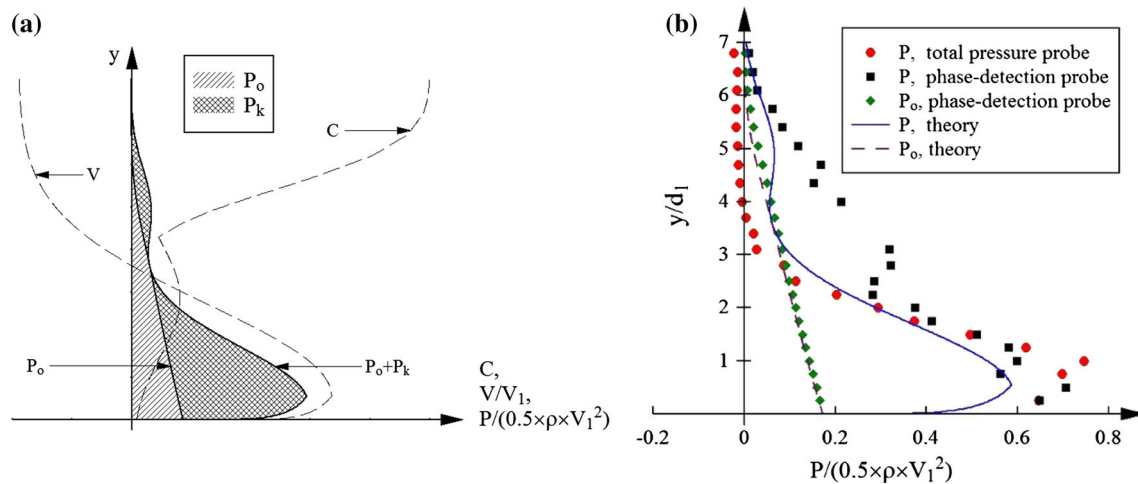


Fig. 8 Theoretical total pressure and piezometric pressure distributions. **a** Sketch of total pressure and piezometric pressure derived from void fraction and interfacial velocity profiles. **b** Comparison

between total pressure data measured with pressure probe and calculated based upon two-phase flow measurements for $Fr_1 = 7.5$, $(x - x_1)/d_1 = 12.5$

$$P_o(y) = \int_y^{Y_{90}} (1 - C) \times \rho \times g \times dy \quad (10)$$

$$P_k(y) = \frac{1}{2} \times (1 - C) \times \rho \times V^2 \quad (11)$$

where ρ is the water density and y is the probe sensor elevation above the invert. Note that Eq. (10) assumes implicitly a hydrostatic pressure distribution in the roller, following limited time-averaged bottom pressure data sets (Rajaratnam 1965; Abdul Khader and Elango 1974; Fiorotto and Rinaldo 1992). In a high-speed flow, the flow velocity can be represented by the interfacial velocity V . The vertical profiles of void fraction C and interfacial velocity V measured with the phase-detection probe followed, respectively, Eqs. (3), (4) (6a) and (6b). Therefore, the total pressure profile was predicted by expressing C and V in Eqs. (9) to (11) with their theoretical solutions. Figure 8a presents a sketch of total pressure profile based upon the void fraction and velocity data, and a comparison between the experimental total pressure data, the calculation based upon two-phase flow measurements and the corresponding theoretical profile is shown in Fig. 8b. Reasonably good agreement was achieved between the data sets in the positive flow region ($y/d_1 < 2.6$ in Fig. 8b). In the recirculation region, the total pressure probe was not aligned against the flow direction and the pressure data were not meaningful: the kinetic pressure component might be missed, and negative pressure relative to atmospheric was sometimes detected when the sensor head was in the wake of the probe itself. The theoretical piezometric pressure P_o given by Eq. (10) is also plotted in Fig. 8, illustrating the proportions of piezometric and kinetic

pressure contributions for the given flow conditions. The piezometric pressure distributions indicated that the pressure gradient was hydrostatic taking into account the air content [Eq. (10)].

Some typical probability density functions (PDFs) of total pressure are presented in Fig. 9. The data were recorded in the shear layer at the characteristic elevations of maximum mean total pressure $Y_{P_{max}}$ and of maximum bubble count rate $Y_{F_{max}}$. Note that the bin sizes of PDF were different for different Froude numbers corresponding to the different pressure ranges. The broader probability distributions indicated larger pressure fluctuations for higher Froude numbers. The smallest Froude number exhibited PDFs close to the normal distribution at both elevations, while the skewness of data increased with increasing Froude number, positive at the lower elevation $Y_{P_{max}}$ and negative at the higher position $Y_{F_{max}}$.

The time-averaged total pressure was derived, and the pressure fluctuation was characterised by the standard deviation of the total pressure. Figure 10 presents the vertical profiles of mean total pressure $P/(0.5 \times \rho \times V_1^2)$ (Fig. 10a) and its fluctuation $p'/(0.5 \times \rho \times V_1^2)$ (Fig. 10b) for all tested flow conditions. Both P and p' presented similar profiles, varying gradually as the distance from the jump toe increased. In the turbulent shear region ($y < y^*$), the mean total pressure distribution was consistent with a superposition of the piezometric pressure and the kinetic pressure, exhibiting a maximum P_{max} at an elevation $0.5 < Y_{P_{max}}/d_1 < 0.9$. The maximum total pressure P_{max} decreased with increasing longitudinal distance, reflecting the dissipation of kinetic energy and turbulence of the flow. The vertical distributions of total pressure fluctuations presented a marked peak at some higher elevations than

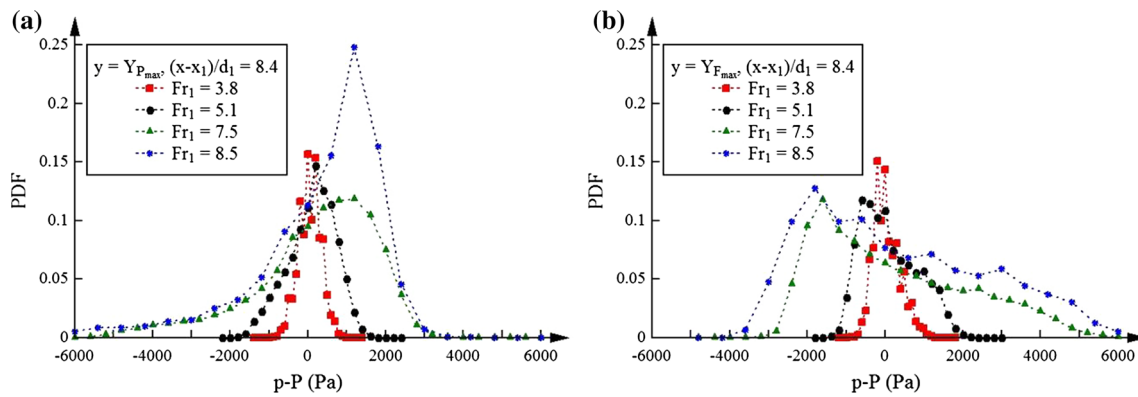


Fig. 9 Probability density functions of instantaneous total pressure deviation from the mean in the shear layer of hydraulic jumps. **a** $y = Y_{P_{\max}}$, $(x - x_1)/d_1 = 8.4$. **b** $y = Y_{F_{\max}}$, $(x - x_1)/d_1 = 8.4$

that of the mean pressure, i.e. $Y_{p'_{\max}} > Y_{P_{\max}}$, corresponding to the occurrence of maximum pressure fluctuations. The magnitude of total pressure fluctuations decreased with increasing distance from the jump toe. The data showed relatively larger pressure fluctuations for higher Froude numbers. In the recirculation region ($y > y^*$), the kinetic pressure component could not be captured accurately by the total pressure probe.

Figures 11a, b presents the dimensionless maximum mean total pressure $P_{\max}/(0.5 \times \rho \times V_1^2)$ and maximum characteristic fluctuation amplitude $p'_{\max}/(0.5 \times \rho \times V_1^2)$ as functions of the relative longitudinal position to roller length. Figure 11a shows a rapid longitudinal decay in maximum total pressure in the first half of jump roller [$0 < (x - x_1)/L_r < 0.5$]. Given the upstream free-stream velocity $U = 1.1 \times V_1$ and $P_{\max}(x = x_1) \sim 0.5 \times \rho \times U^2$, the data were correlated as:

$$\frac{P_{\max}}{\frac{1}{2} \times \rho \times V_1^2} = 1.2 \times \exp\left(-\frac{1}{5 \times (Fr_1 - 1)} \times \frac{x - x_1}{d_1}\right) \quad \text{for } 0 < \frac{x - x_1}{L_r} < 0.5 \quad (12)$$

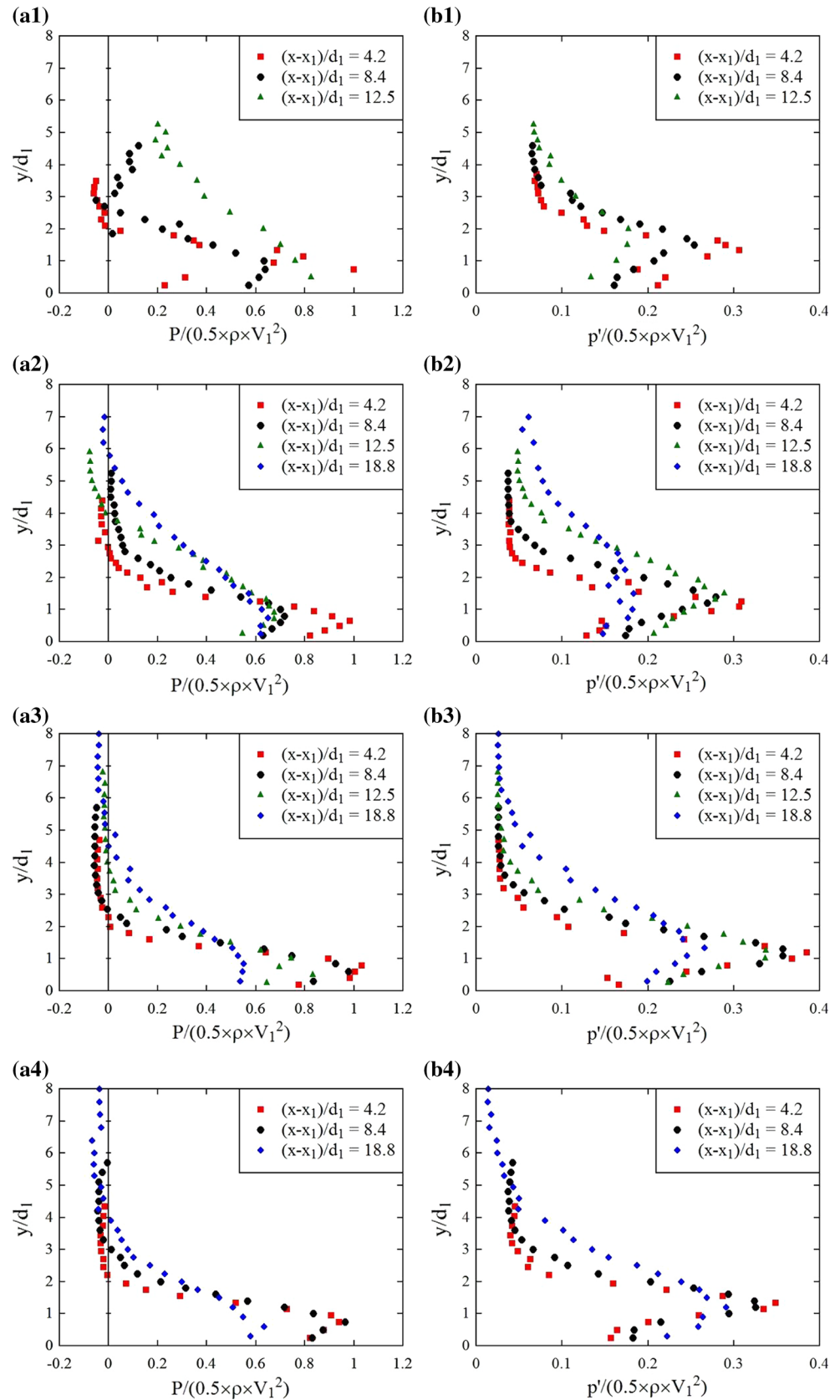
Equations (8) and (12) imply similar decreasing trends in maximum velocity and total pressure in the first half of the roller. In the second half roller, the decay rate of P_{\max} became smaller, as the increase in piezometric pressure and the decrease in kinetic pressure were quantitatively comparable. Momentum considerations indicated that the dimensionless downstream total pressure level differed for different Froude numbers. The maximum standard deviations of pressure showed a constant decreasing rate over the full roller length (Fig. 11b). The linear trend was best fitted by Eq. (13) with the roller length expressed as a function of the Froude number:

$$\frac{p'_{\max}}{\frac{1}{2} \times \rho \times V_1^2} = 0.385 - \frac{1}{25 \times (Fr_1 - 1)} \times \frac{x - x_1}{d_1} \quad \text{for } 0 < \frac{x - x_1}{L_r} < 1 \quad (13)$$

The vertical positions of maximum mean total pressure $Y_{P_{\max}}$ and maximum total pressure fluctuation $Y_{p'_{\max}}$ are compared in Fig. 12 with those of maximum bubble count rate $Y_{F_{\max}}$ and maximum interfacial velocity $Y_{V_{\max}}$. The data showed relationships $Y_{V_{\max}} \approx Y_{P_{\max}} < Y_{p'_{\max}} < Y_{F_{\max}}$. The maximum mean total pressure and velocity were observed at close elevations, though little variation was seen in $Y_{P_{\max}}$ at different longitudinal positions whereas $Y_{V_{\max}}$ increased slightly along the roller. Both total pressure fluctuations and bubble count rate were turbulence-related processes and linked with the local turbulence intensity. The different characteristic elevations $Y_{p'_{\max}} < Y_{F_{\max}}$ suggested that the two processes were not directly associated, because the bubble count rate also relied upon the local void fraction and affected by buoyancy.

In such a highly turbulent flow, the total pressure fluctuations must be contributed to some extent by the velocity turbulence, especially in the high-speed flow region. Figure 13 presents a comparison between the relative total pressure fluctuation to the local kinetic pressure $p'/(0.5 \times \rho \times V^2)$ and the square of turbulence intensity $Tu^2 = v'^2/V^2$ in the turbulent shear region ($0 < y < y^*$), where V is the local mean velocity. The decomposed high-frequency turbulence intensity Tu''^2 is also compared. The data showed that the relative total pressure fluctuation increased with increasing distance from the invert to the elevation of maximum bubble count rate $Y_{F_{\max}}$ and decreased further above, with the maximum smaller than unity. At the given position $(x - x_1)/d_1 = 8.4$, the magnitude of turbulence intensities Tu and Tu'' varied for different flow conditions depending upon the extent of

Fig. 10 Vertical distributions of mean total pressure **a1–a4** and total pressure fluctuations **b1–b4**. **a1** $Fr_1 = 3.8$ **b1** $Fr_1 = 3.8$ **a2** $Fr_1 = 5.1$ **b2** $Fr_1 = 5.1$ **a3** $Fr_1 = 7.5$ **b3** $Fr_1 = 7.5$ **a4** $Fr_1 = 8.5$ **b4** $Fr_1 = 8.5$



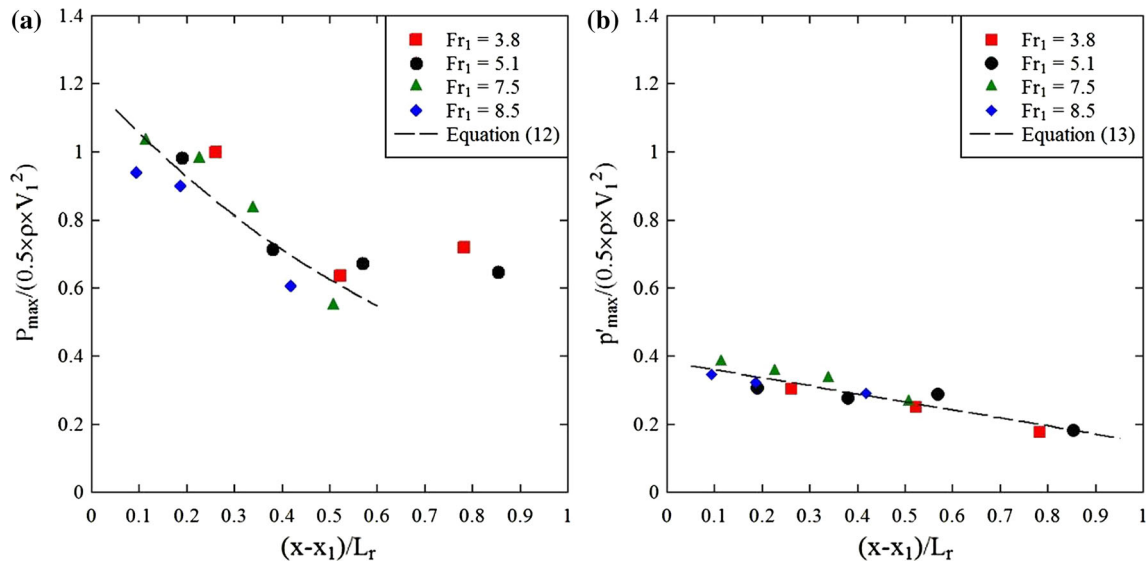


Fig. 11 Longitudinal decay in maximum mean total pressure and total pressure fluctuation. **a** Dimensionless maximum mean total pressure. **b** Dimensionless maximum total pressure fluctuation

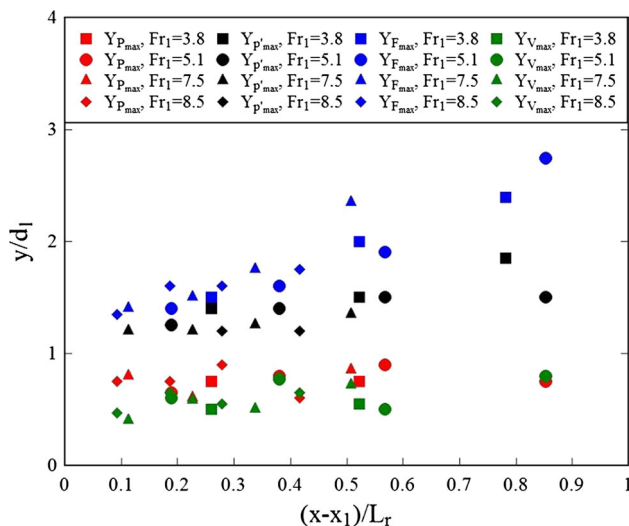


Fig. 12 Comparison between characteristic elevations of maximum mean total pressure Y_{Pmax} , maximum total pressure fluctuation $Y_{P' max}$, maximum bubble count rate Y_{Fmax} and maximum interfacial velocity Y_{Vmax}

longitudinal turbulence dissipation. Tu^2 was typically larger than the relative pressure fluctuation, while the relationship between Tu'^2 and $p'/(0.5 \times \rho \times V^2)$ varied with Froude numbers. The data distributions suggested possible correlations between the relative fluctuations in total pressure and velocity in the lower part of the shear flow ($0 < y < Y_{Fmax}$). Visual observation indicated that such a flow region was a low-aerated, high-speed layer between the channel bed and the path of large-size vortical structures.

4 Discussion: characteristic total pressure fluctuation frequencies

The instantaneous total pressure signals exhibited some pseudo-periodic patterns. For example, Fig. 14 presents a typical signal in the turbulent shear region, sampled at 5 kHz. The low-pass-filtered signals with cut-off frequencies of 25 and 5 Hz, respectively, highlighted some low-frequency patterns. The cut-off frequencies were selected to best outline the fluctuating patterns in a range of scales. The characteristic frequencies of the wavelike filtered signals were analysed manually at the elevation of maximum bubble count rate (Y_{Fmax}). The manual data processing guaranteed maximum reliability of the results.

The analysed characteristic total pressure fluctuation frequencies are summarised in Table 2. The relatively high-frequency filtered signals (0–25 Hz) exhibited a range of typical fluctuation frequencies $F_p^{(H)}$ between 8 and 12 Hz, whereas the low-frequency filtered signals (0–5 Hz) gave a frequency $F_p^{(L)}$ about 2.6 Hz. The upper and lower characteristic frequencies are plotted in Fig. 15a, b, respectively, at the relative longitudinal positions in jump roller. Figure 15a shows a smaller dimensionless frequency $F_p^{(H)} \times d_1/V_1$ for a higher Froude number, which decreased with increasing distance from the jump toe. The data are compared with the longitudinal distributions of bubble cluster count rate $F_{clu} \times d_1/V_1$ at the same elevation. The comparable decreasing trends along the roller might suggest some correlation between the detected pressure fluctuations and the turbulent air–water flow features, of which the longitudinal decay was related to the diffusion and dispersion of bubbly flow structures as well as the

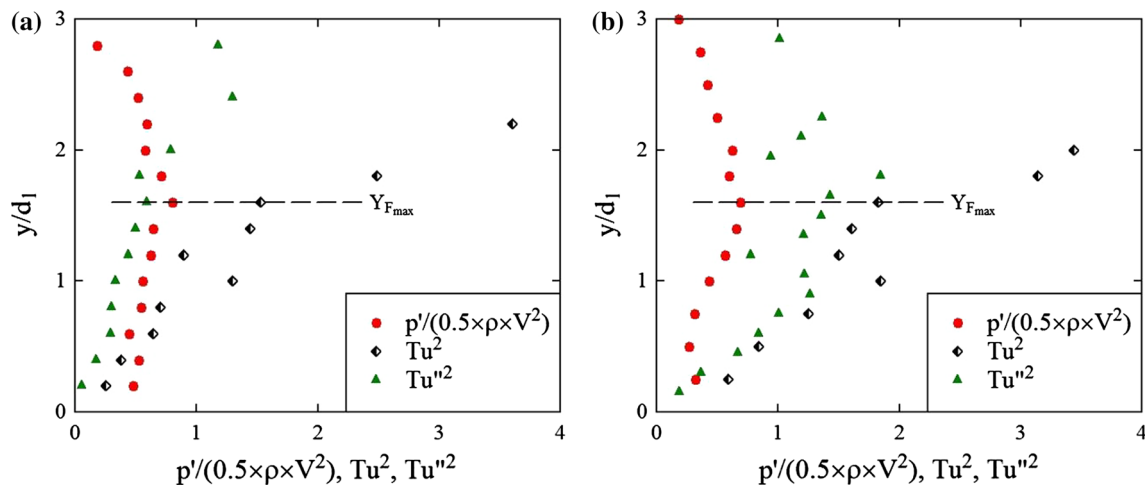


Fig. 13 Comparison between relative total pressure fluctuation and square of turbulence intensities for raw and high-frequency signals in the turbulent shear region. **a** $Fr_1 = 5.1$, $(x - x_1)/d_1 = 8.4$. **b** $Fr_1 = 8.5$, $(x - x_1)/d_1 = 8.4$

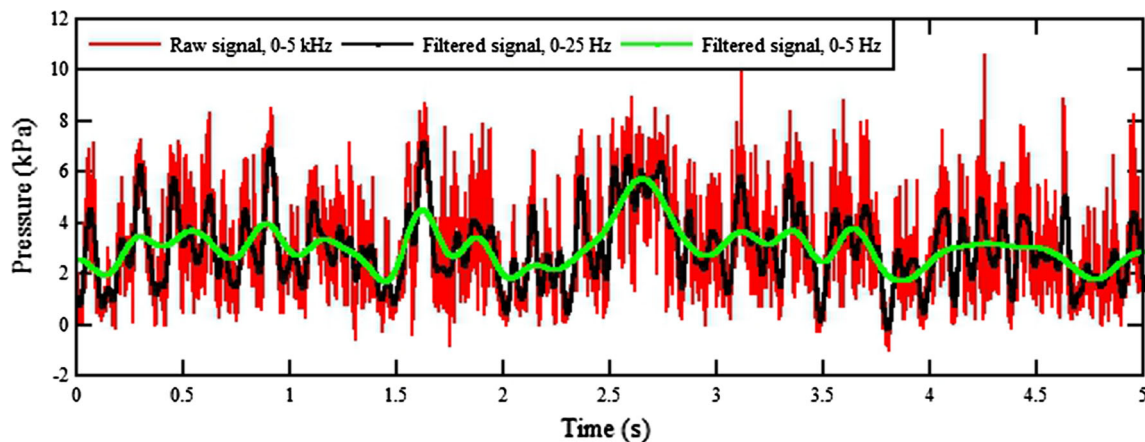


Fig. 14 Raw and low-pass-filtered total pressure signals recorded in the shear layer—flow conditions: $Q = 0.0347 \text{ m}^3/\text{s}$, $d_1 = 0.02 \text{ m}$, $x_1 = 0.83 \text{ m}$, $Fr_1 = 7.5$, $x - x_1 = 0.167 \text{ m}$, $y = 0.03 \text{ m}$

turbulence dissipation. In this case, this high-frequency total pressure fluctuation was mainly linked to the fast variation in kinetic pressure. Such type of fluctuations could correspond to the relatively large-scale turbulent behaviours, or their accumulative effect. For example, it was possible that only bubble clusters larger than a certain size were responsible to the kinetic pressure fluctuations. Correlation between total pressure probe and phase-detection probe signals indicated an instantaneous pressure drop corresponding to an instantaneous increase in void fraction, thus a detection of air. It is noteworthy that the variation of cluster count rate F_{clu} with Reynolds number was significant, whereas the corresponding difference in pressure fluctuation frequency $F_p^{(H)}$ was limited.

On the other hand, the lower characteristic frequencies $F_p^{(L)}$ were about constant independently of longitudinal positions and flow conditions, while the dimensionless

frequency $F_p^{(L)} \times d_1/V_1$ decreased with increasing Froude number (Fig. 15b). This relatively low characteristic fluctuation frequency was of the same order of magnitude as some slow fluctuating motions of the jump such as the free-surface fluctuations, longitudinal jump toe oscillations and formation of large-size vortices. Figure 15b compares the frequencies $F_p^{(L)}$ with the characteristic free-surface fluctuation frequencies F_{fs} measured simultaneously with acoustic displacement meters. The close frequency data for a range of flow conditions suggested that the lower range of total pressure fluctuations were predominantly affected by the fluctuations in free-surface elevation, thus the piezometric pressure term. Correlation between the signals of total pressure probe and acoustic displacement meter (both filtered with 50 Hz cut-off frequency) showed strong coupling between the pressure and water level variations in the upper turbulent shear layer where large-scale

turbulence developed. In the lower shear region with large velocity, their interaction became weak, and the change of total pressure was associated with the kinetic pressure fluctuation.

5 Conclusion

The total pressure and air–water flow properties were measured simultaneously at adjacent locations in hydraulic

Table 2 Characteristic total pressure fluctuation frequencies based upon a manual processing of two low-pass filtered signals—data recorded in the turbulent shear layer at $y = Y_{Fmax}$

Q (m ³ /s)	d_1 (m)	x_1 (m)	Fr_1 (—)	Re (—)	$x - x_1$ (m)	$F_p^{(H)}$ (Hz)	$F_p^{(L)}$ (Hz)
0.0179	0.0206	0.83	3.8	3.5×10^4	0.083	11.07	2.59
					0.167	9.05	2.64
					0.250	8.35	2.61
0.0239	0.0209	0.83	5.1	4.8×10^4	0.083	12.02	2.59
					0.167	10.32	2.65
					0.250	8.78	2.58
0.0347	0.0206	0.83	7.5	6.8×10^4	0.083	11.93	2.59
					0.167	11.18	2.64
					0.250	9.85	2.50
0.0397	0.0208	0.83	8.5	8.0×10^4	0.083	13.02	2.52
					0.167	11.83	2.63
					0.250	10.18	2.38
					0.375	9.30	2.50

jump rollers, together with the water level fluctuations above. Four Froude numbers were investigated with the same intake aspect ratio and inflow length, corresponding to partially developed inflow conditions.

The two-phase flow measurements provided typical time-averaged void fraction and bubble count rate distributions. The data distributions reflected the singular air entrainment at the jump toe and the air–water exchange next to the free surface. Comparison between the present results recorded at 5 kHz sampling rate for 180 s and some previous data at 20 kHz for 45 s showed coincidence in terms of the time-averaged void fraction. The bubble count rate was, however, underestimated when the Froude and Reynolds numbers were large. The bubble cluster count rate appeared to be proportional to the bubble count rate. The void fraction and interfacial velocity followed theoretical solutions, where some characteristic values were specified with experimental data. The turbulence intensity reflected a combination of fast turbulent and slow fluctuating motions of the flow, and the ‘true’ turbulence was characterised based upon the decomposed high-frequency phase-detection signal.

The total pressure measurements were validated in the turbulent shear region. The total pressure was predicted based upon the void fraction and velocity data, and the predictions agreed well with experimental results given by the total pressure probe. The piezometric pressure exhibited a hydrostatic distribution in the jump roller, taking into account the void fraction distribution. The total pressure distributions presented some marked maximum in the shear flow region. The maximum mean total pressure and maximum pressure fluctuations were observed at different

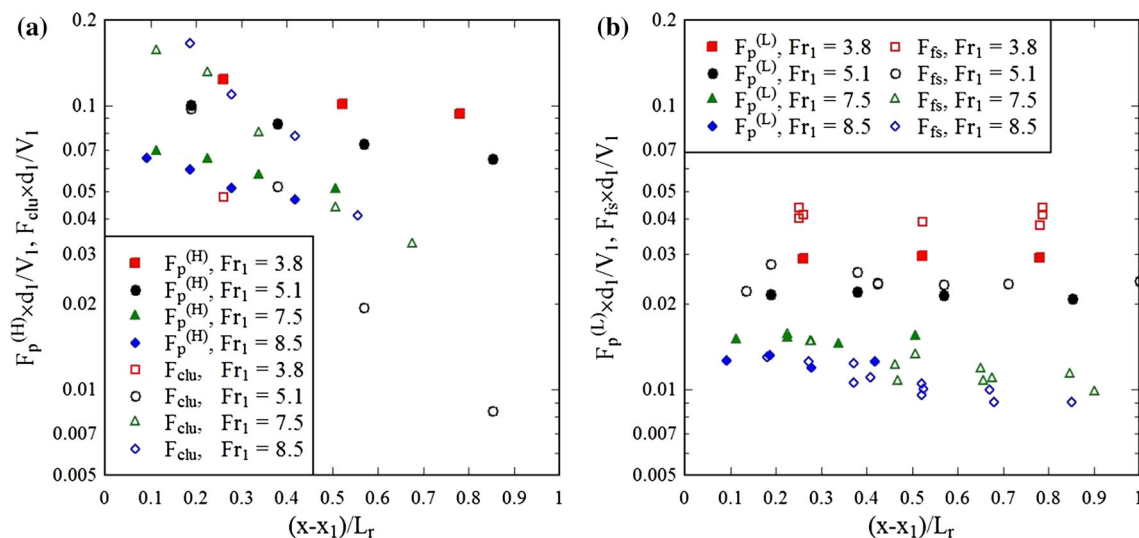


Fig. 15 Longitudinal variations of dimensionless characteristic frequencies of total pressure fluctuations in the turbulent shear layer; data at $y = Y_{Fmax}$. **a** Upper pressure fluctuation frequency $F_p^{(H)}$

compared with bubble cluster count rate F_{clu} . **b** Lower pressure fluctuation frequency $F_p^{(L)}$ compared with free-surface fluctuation frequency F_{fs}

vertical positions. The total pressure fluctuations were associated with both velocity and water level fluctuations. This was supported by comparison between relative total pressure fluctuation and turbulence intensity, and a preliminary investigation of pressure fluctuation frequencies.

Acknowledgments The financial supports of the Australian Research Council (Grant DP120100481) and ESTACA (France) are acknowledged.

References

- Abdul Khader MH, Elango K (1974) Turbulent pressure field beneath a hydraulic jump. *J Hydraul Res* 12(4):469–489
- Brattberg T, Chanson H, Toombes L (1998) Experimental investigations of free-surface aeration in the developing flow of two-dimensional water jets. *J Fluids Eng Trans ASME* 120(4):738–744
- Chanson H (1995) Air entrainment in two-dimensional turbulent shear flows with partially developed inflow conditions. *J Multiphase Flow* 21(6):1107–1121
- Chanson H (1997) Air bubble entrainment in free-surface turbulent shear flows. Academic Press: London, 401 pages
- Chanson H (2007) Bubbly flow structure in hydraulic jump. *Eur J Mech B Fluids* 26(3):367–384
- Chanson H, Carosi G (2007) Turbulent time and length scale measurements in high-velocity open channel flows. *Exp Fluids* 42(3):385–401. doi:[10.1007/s00348-006-0246-2](https://doi.org/10.1007/s00348-006-0246-2)
- Chanson H, Chachereau Y (2013) Scale effects affecting two-phase flow properties in hydraulic jump with small inflow Froude number. *Exp Thermal Fluid Sci* 45:234–242
- Chanson H, Toombes L (2002) Air-water flows down stepped chutes: turbulence and flow structure observations. *Int J Multiph Flow* 28(11):1737–1761
- Cox D, Shin S (2003) Laboratory measurements of void fraction and turbulence in the bore region of surf zone waves. *J Eng Mech* 129:1197–1205
- Crank J (1956) The mathematics of diffusion. Oxford University Press, London
- Fiorotto V, Rinaldo A (1992) Fluctuating uplift and lining design in spillway stilling basins. *J Hydraul Eng* 118(4):578–596
- Kucukali S, Chanson H (2008) Turbulence measurements in hydraulic jumps with partially-developed inflow conditions. *Exp Thermal Fluid Sci* 33(1):41–53
- Liggett JA (1994) Fluid Mechanics. McGraw-Hill, New York
- Lighthill J (1978) Waves in fluids. Cambridge University Press, Cambridge
- Long D, Rajaratnam N, Steffler PM, Smy PR (1991) Structure of flow in hydraulic jumps. *J Hydraul Res IAHR* 29(2):207–218
- Lopardo RA (2013) Extreme velocity fluctuations below free hydraulic jumps. *J Eng*, Hindawi Publishing Corporation, Article ID 678065
- Lopardo RA, Henning RE (1985) Experimental advances on pressure fluctuations beneath hydraulic jumps. Proceedings of 21st IAHR Biennial Congress, Melbourne, Australia, pp 633–637
- Lopardo RA, Romagnoli M (2009) Pressure and velocity fluctuations in stilling basins. Advances in water resources and hydraulic engineering, Proceedings of 16th IAHR–APD congress and 3rd IAHR international symposium on hydraulic structures ISHS, Nanjing, China
- Murzyn F, Chanson H (2008) Experimental assessment of scale effects affecting two-phase flow properties in hydraulic jumps. *Exp Fluids* 45(3):513–521
- Murzyn F, Chanson H (2009) Experimental investigation of bubbly flow and turbulence in hydraulic jumps. *Environ Fluid Mech* 9(2):143–159. doi:[10.1016/j.expthermflusc.2009.06.003](https://doi.org/10.1016/j.expthermflusc.2009.06.003)
- Murzyn F, Mouaze D, Chaplin JR (2005) Optical fibre probe measurements of bubbly flow in hydraulic jumps. *Int J Multiph Flow* 31(1):141–154
- Murzyn F, Mouaze D, Chaplin JR (2007) Air-water interface dynamic and free surface features in hydraulic jumps. *J Hydraul Res IAHR* 45(5):679–685
- Narayanan R (1980) Cavitation induced by turbulence in stilling basin. *J Hydraul Div* 106:616–619
- Onitsuka K, Akiyama J, Shige-eda M, Ozeki H, Gotoh S, Shiraishi T (2009) Relationship between pressure fluctuations on the bed wall and free surface fluctuations in weak hydraulic jump. In: Proceedings of the fifth international conference on fluid mechanics (Shanghai, China, 2007), pp 300–303. doi:[10.1007/978-3-540-75995-9_96](https://doi.org/10.1007/978-3-540-75995-9_96)
- Peterka AJ (1958) Hydraulic design of stilling basins and energy dissipators. US Bureau of Reclamation Engineering Monograph 25. US Department of the Interior, Washington
- Rajaratnam N (1962) An experimental study of air entrainment characteristics of the hydraulic jump. *J Instr Eng India* 42(7):247–273
- Rajaratnam N (1965) The hydraulic jump as a wall jet. *J Hydraul Div ASCE* 91(HY5):107–132
- Rajaratnam N (1967) Hydraulic jumps. In: Chow VT (ed) Advances in hydrosience, vol 4. Academic Press, New York, USA, pp 197–280
- Resch FJ, Leutheusser HJ (1972) Le ressaut hydraulique: mesure de turbulence dans la région diphasique. *Journal La Houille Blanche* 4:279–293 (in French)
- Richard GL, Gavriluk SL (2013) The classical hydraulic jump in a model of shear shallow-water flows. *J Fluid Mech* 725:492–521. doi:[10.1017/jfm.2013.174](https://doi.org/10.1017/jfm.2013.174)
- Riegel RM, Beebe JC (1917) The hydraulic jump as a means of dissipating energy. Miami Conservancy District, Technical reports part III: 60–111. Dayton (Ohio)
- Roache PJ (2009) Perspective: validation—what does it mean?. *J Fluids Eng*, ASME 131: Paper 034503
- Schiebe F (1971) The stochastic characteristics of pressure fluctuations on a channel bed due to the turbulence in a hydraulic jump. PhD thesis, The University of Minnesota, Minneapolis, US
- Thandaveswara BS (1974) Self aerated flow characteristics in developing zones and in hydraulic jumps. PhD thesis, Dept. of Civil Engineering, Indian Institute of Science, Bangalore, India, 399 pages
- Toombes L (2002) Experimental study of air-water flow properties on low-gradient stepped cascades. PhD Thesis, Dept. of Civil Engineering, The University of Queensland, Brisbane, Australia
- Vasiliev OF, Bukreyev VI (1967) Statistical characteristics of pressure fluctuations in the region of hydraulic jump. Proceedings of the congress—international association for hydraulic research 2:1–8
- Wang H, Chanson H (2014) Air entrainment and turbulent fluctuations in hydraulic jumps. *Urban Water J*. doi:[10.1080/1573062X.2013.847464](https://doi.org/10.1080/1573062X.2013.847464)
- Wang H, Felder S, Chanson H (2014) An experimental study of turbulent two-phase flow in hydraulic jumps and application of a triple decomposition technique. *Exp Fluids* 55(7):1–18. doi:[10.1007/s00348-014-1775-8](https://doi.org/10.1007/s00348-014-1775-8)